Hindawi
Journal of Nanomaterials
Volume 2022, Article ID 9530499, 11 pages
https://doi.org/10.1155/2022/9530499

Research Article

Influence of Different Frequency Pulse on Weld Bead Phase Ratio in Gas Tungsten Arc Welding by Ferritic Stainless Steel AISI-409L

R. Venkatesh,[1] **S. Manivannan**,[2] **S. Kaliappan**,[3] **S. Socrates**,[3] **S. Sekar**,[4] **Pravin P. Patil**,[5] **L. Natrayan**,[1] **and Melkamu Beyene Bayu**[6]

[1]*Department of Mechanical Engineering, Saveetha School of Engineering, SIMATS, Chennai, Tamil Nadu 602105, India*
[2]*Centre for Material Science, Department of Mechanical Engineering, Karpagam Academy of Higher Education, Coimbatore, Tamil Nadu, India*
[3]*Department of Mechanical Engineering, Velammal Institute of Technology, Chennai, 601204 Tamil Nadu, India*
[4]*Department of Mechanical Engineering, Rajalakshmi Engineering College, Rajalakshmi Nagar, Thandalam, Chennai, 602105 Tamil Nadu, India*
[5]*Department of Mechanical Engineering, Graphic Era Deemed to be University, Bell Road, Clement Town, 248002 Dehradun, Uttarakhand, India*
[6]*Department of Mechanical Engineering, Ambo Institute of Technology–19, Ambo University, Ethiopia*

Correspondence should be addressed to R. Venkatesh; venkidsec@gmail.com, S. Manivannan; manivannan.s@kahedu.edu.in, L. Natrayan; natrayanmech007@gmail.com, and Melkamu Beyene Bayu; melkamu.beyene@ambou.edu.et

Received 12 April 2022; Revised 13 May 2022; Accepted 30 May 2022; Published 17 June 2022

Academic Editor: S.K. Khadheer Pasha

Copyright © 2022 R. Venkatesh et al. This is an open access article distributed under the Creative Commons Attribution License, which permits unrestricted use, distribution, and reproduction in any medium, provided the original work is properly cited.

The objective of the present experimental work is to obtain an appropriate welding parameter on pulsed current gas tungsten arc welding (GTAW) ferritic stainless steel AISI 409L with a thickness of 4.5 mm. Frequency affected penetration, and the ratio of bead width to penetration (aspect ratio) is the main objective of the research. A Taguchi L9 orthogonal array with three level four factors was chosen to execute the bead on plate welding. It leads to optimize the input process parameters on main effect plot via analysis of variance, and it has imposed to determine their contribution level of each parameter with respect to responses. Taguchi optimized conditions for butts weld with the pulsed TIG and its surface morphology, and mechanical characteristics of AISI 409L weld was investigated. A full penetration with an optimal aspect ratio was accomplished using high-frequency pulsing, according to the findings. The mechanical properties were characterized using Vickers microhardness and tensile tests on the base material and weld metals. Microstructural study revealed that these variables have a greater impact on the bead profile. Pulsed TIG showed maximum UTS of 445 MPa and a minimum of 385 MPa, with an average of three samples of 415 MPa. The weld metal in all of the zones had influenced superior tensile strength (UTS) as compared to base metal, according to the findings. The obtained strain percentage for both butt and TIG welds, however, was smaller than that of the parent metal. The formation of martensitic was attributed for the higher tensile strength with minimized ductility of the pulsed TIG welds. Furthermore, results on the hardness are in concurrence with the tensile experiments, as the zone for fusion has a higher hardness than the base metal. Corrosion behavior of the parent metal and welded specimen was analyzed using a potentio-dynamic polarization technique. The electrochemical behavior of base material and weld samples confirmed that the overall corrosion resistance is better in parent material than the other zones.

1. Introduction

Welding is the most common technique to join the two similar or dissimilar materials by heat and/or pressure to fuse by surface contact between the materials on various industrial fabrication applications like sinks, containers for chemical and transport industries, food processing, and fasteners. The samples are joined by the technique to melt at the interface during welding influence permanent union to be established following solidification. The filler material is needed to be used to create a weld pool effect on molten material, which solidifies to make a good bonding between the surfaces. The modified microstructure results, based the mechanical properties, are to be evaluated. The hardness of weld zone may be varied due to the lack of solidification; oxidation during the high temperature leads crack tendency on the weld joint. All have an impact on a material's weldability. The efficiency of pulsed TIG welding parameters was examined by Chennaiah et al. [1]. They claimed that distortion is the primary issue with thin sections. Fusion zone grain refinement, reduced heat sensitivity with minimized area of HAZ, low deformation on high residual stress, and limited segregation are the metallurgical benefits of pulsed TIG welding [2]. Indira Rani and Marpu [3] studied the effect of 70-74 amps current and 700-760 rpm travel speed with 3 to 7 Hz pulse frequency on weld joint. They found that both yield and tensile strengths of weld joint are similar to parent metal. It was due to the connection failure on heat-affected zone in the weldments. The laser, tungsten inert gas arc, and hybrid tungsten inert gas arc welding are fusion welding technologies that are similar to low-heat-input welding [4]. It was due to the reason for high power density, these techniques generate less metallurgical distortion in the work piece and, as a result, produce higher-quality welds than other processes [5]. Finally, using the pulsed TIG welding process is to rectify the inadequacy of thermal and mechanical characteristics [6]. The scope of this present study is to find the optimum input process parameter for GTAW of ferritic stainless steel AISI 409 with a thickness of 4.5 mm. It characterized study on the micro and macrostructural aspects of welded samples and measured the bead shape (using welding expert software). Taguchi analysis is imposed to optimize input process parameters by main effect plots, while ANOVA is implemented to determine the contribution level percentage for each element characterized with corresponding responses.

2. Experiment Design Utilizing the Taguchi Method

A 4 factor–3 level Taguchi design was utilized in this investigation, resulting in 8 degrees of freedom (DOF) [$DOF = no.\text{of}\, factors\,(no.\text{of}\, levels)$]. In the present 4×3 design combinations, full factorial experimentation necessitates $(34 = 81)$ total experiments, which is laborious and time demanding. Hence, instead of 81 experiments, Taguchi L9 orthogonal array is utilized to analyze the main impacts in above-mentioned (9) experiments. The optimum value is calculated using the Taguchi method by the signal to noise ratio (S/N ratio). It is categorized into three major systems such as lower is better, nominal is better, and higher is better. Performance factors like bead width and depth of penetration were chosen in the present investigation [7]. Bead width is defined as a nondesirable parameter, while depth of penetration is regarded good. As a result seen from S/N ratio graph, the lower the better criterion was chosen for the aspect ratio (W/P). For the value as lower is the better criteria, the S/N ratio equation is as follows:

$$\mathrm{SN} = -10 \log_{10} \frac{1}{n \sum ni} = 1 Yi^2, \tag{1}$$

where n is the number of times an experimental combination has been repeated and Yi denotes the performance value of the i^{th} experiment. The mean value of the S/N ratio has computed at each and every level of the four parameters [8]. The optimum level of related factor has chosen as the one with the higher is the best for mean (S/N) value among all three levels.

3. Experimental Procedure

The ferritic stainless steel AISI409L with 4.3 mm thickness has been considered for the study. Its chemical composition is confirmed by using optical emission spectroscopy which is noted in Table 1. Five samples (100 mm × 50 mm × 4.3 mm) were prepared from rolled plate. Prepared plates were welded with a Kemppi Master make TIG MLS 4000 series and a pulsed current GTAW method [9]. During the welding process, argon shielding gas supplied with the flow rate of 10-15 lpm. The experiments in this study were designed by ANNOVA Taguchi design (L9). The 9 investigations were obtained by means of L9 orthogonal array to examine the effect on impacting weld process factors [10]. The influence of low and high frequency on the process variables was investigated in a total of 18 trials. The four most significant PCGTAW parameters were chosen [11]. The range of each process parameter level was determined using trial welds, and the process parameters employed, like IB, IP, peak, and frequency, are detailed in Table 1. Before welding, the heat input necessary for each welding experiment was calculated using the process parameters listed above to confirm the input (heat) having the allowable boundary. The following equation is used to compute input heat [12].

$$\mathrm{HI} = \eta \frac{\mathrm{Im}\, xV}{\mathrm{SJ/mm}}. \tag{2}$$

It was calculated from applied current and pulsed high to low frequency during PCGTAW; avg current has used to measure the input heat. The below equation is used to compute the mean current Im.

$$\mathrm{Im} = \frac{(\mathrm{Ip}) + (\mathrm{Ibxtb})}{\mathrm{tp} + \mathrm{tb}}. \tag{3}$$

Here, Ip denotes the peak current, Ib denotes the base current, and tp and tb denote the peak and base current

Table 1: Chemical compositions of AISI 409L using OES.

Element	C	Cr	Ni	Nb	Cu	Si	Mn	P	S	Co	Ti	Fe
Wt. %	0.02	11.5	0.3	0.02	0.1	0.4	1.0	0.02	0.4	0.02	0.03	Bal.

Table 2: Taguchi design: level and factors.

Factors/ level	Peak current (Ip) in amps	Base current (Ib) in amps	Peak in (%)	Low frequency (f) in Hz	High frequency (f) in Hz
Level 1	200	60	40	6	150
Level 2	220	80	50	8	200
Level 3	240	100	60	10	250

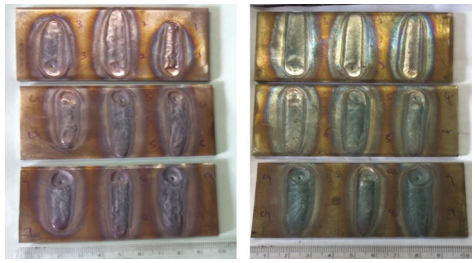

Figure 1: The welded specimen at different frequency parameter.

durations, respectively. PCGTA welding has performed on 409L plates under high frequency based on the different levels of parameters developed utilizing the L9 orthogonal array [13]. In the investigation, peak frequency levels such as 150, 200, and 250 Hz were used. Table 2 lists the input process parameter with their interaction for the HF. Wire EDM was used to cut samples of 25 mm length from all of the weld beads in order to examine the crossed section and assess the bead type profile [14]. The prepared samples are polished according to surface morphology examinations. The prepared test samples are etched by Vilella reagent (3 g picric acid +15 ml hydrochloric acid +200 ml ethanol) and bead profiles were studied with a Leica Inverted microscope. Welding expert software was from Strauss Inc. [15]. Table 1 shows the chemical compositions of AISI 409L using optical emission spectroscopic (OES) techniques (Test Point, Coimbatore, Tamil Nadu, India).

In the studies, TIG welding with a pulsed DC mode was utilized because it concentrates the heat in one cycle to complete the weld and allows solidification in the next cycle. This experiment used tungsten electrodes with a diameter of 1.6 mm that had been thoriated [16]. The electrode's end prepared through grinding with tip dia down to 2/3 of its actual size, and then, it is striking an arc on a fragment piece of material. The ball forms at the electrode's end. In general, an electrode that has small and welding current has produces an abnormally huge ball. However, the electrode that is too large will produce no ball at all [17].

A number of experimental tests were conducted prior to the real experiment to determine the proper parameter range in which welding could be performed without apparent defects such as undercutting and porosity. After the trail welds on the AISI 4 09L plates were completed, they were allowed to cool before removing the welded area with a wire brush and cleaning it [18]. In addition ($100 \times 50 \times 4.5\,mm^3$), crosssection specimens were cut from each sample for microstructural research and microhardness evaluation. Crosssection of the welded specimen has placed and polished with different grades (1/0, 2/0, 3/0, 4/0, and 5/0) of emery polishing paper successively before micro and macroanalytical measurement. Microhardness was assessed after the obtained samples were etched with electrolytic reagent and used for micro and macrostructural studies [19].

L9 plates were allowed to cool before the welded portion was removed and cleaned with a wire brush. In addition ($100 \times 50 \times 4.5\,mm^3$), crosssection specimens were cut from each sample for microstructural research and microhardness evaluation [20]. Crosssection of the welded specimen has placed and polished with different grades (1/0, 2/0, 3/0, 4/0, and 5/0) of emery polishing paper successively before micro and macroanalytical measurement. Microhardness was assessed after the obtained samples were etched with electrolytic reagent and used for micro and macrostructural studies. Microhardness was assessed after the obtained samples were etched with electrolytic reagent and used for micro and macrostructural studies. The tensile test samples are prepared as per ASTM E8 Standards, the Tinius Olsen makes electromechanical configured UTM machine used for mechanical characteristic evaluation. The hardness variance in the parent metal (BM), heat affected zone (HAZ), and weld meta (WM) regions is determined using a micro-Vickers hardness tester [21].

4. Result and Discussion

Welding of AISI 409L samples was done in this investigation utilizing a pulsed TIG welding method with three levels of four parameters, 120 mm/min welding speed, and argon as a shielding gas. This study is carried out in two stages [22]. Whereas in the first phase, beads are created on an AISI 409L plate, let to cool, and then, micro and macroanalysis is performed to determine the most optimized parameter among them. Weld joint and microstructure were produced once the optimal parameter was acquired [23]. The mechanical parameters of this welded specimen, such as tensile and hardness surveys, were examined. The finished welded sample and base material were also subjected to electrochemical tests.

4.1. Macrostructural Analysis. For welding expert equipment, samples were prepared according to established metallographic processes. The bead on plate welds revealed good weld beads and satisfactory weld quality. All of the sample's macrostructures are observed in 50x magnification and are shown here, together with penetration depth and variation in bead width, in order to determine the best aspect

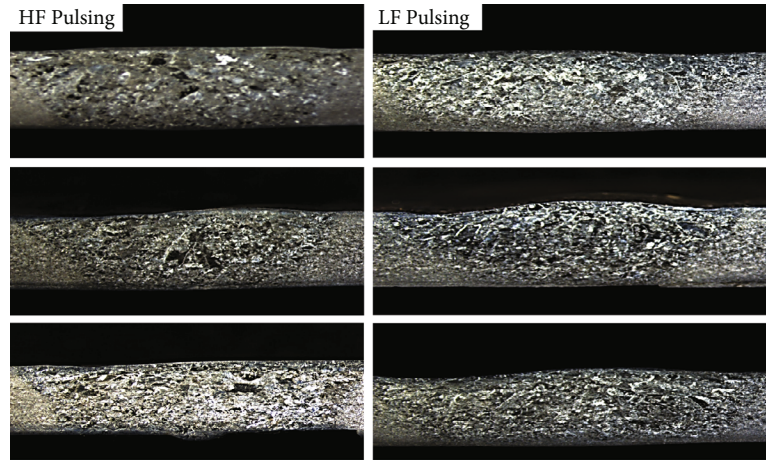

Figure 2: Macrograph and bead profile of PC-GTAW based on penetration rate in mm (P), width of weld in mm (W), depth to width ratio of weld (W/P), and input heat (HI) in J/mm (50x magnification).

Table 3: Taguchi experimental results with their responses related to HF pulsing for bead geometry.

S. no.	Ip	Ib	Peak%	Frequency (Hz)	AR	SNRA1	MEAN1	Depth (mm)	Heat input (J/mm)
	200	60	40	150	3.27	-10.291	1.87	2.25	466.9
	200	80	50	200	2.23	-6.9661	1.82	4.2	621.25
	200	100	60	250	2.31	-7.272	2.26	4.1	749
	220	60	50	250	1.93	-5.7111	1.81	4.2	728
	220	80	60	150	2.44	-7.7478	1.82	4.26	777.3
	220	100	40	200	2.33	-7.3471	1.68	4.11	695
	240	60	60	200	2.47	-7.8539	1.9	4.32	845
	240	80	40	250	2.40	-7.604	2.36	4.1	695
	240	100	50	150	2.44	-7.747	2.12	4.52	893.2

Table 4: Taguchi L9 orthogonal array and experimental results of LF pulsing for bead geometry and their corresponding S/N values and heat inputs.

S. no.	Ip	Ib	Peak%	Frequency (Hz)	AR	SNRA1	MEAN1	Depth (mm)	Heat input (J/mm)
	200	60	40	150	3.29	-10.291	1.87	2.2	450
	200	80	50	200	2.50	-6.9661	1.82	3.56	607
	200	100	60	250	2.48	-7.2722	2.26	4.14	744.8
	220	60	50	250	2.25	-5.7111	1.81	4.25	625.6
	220	80	60	150	2.44	-7.7478	1.82	4.26	783.2
	220	100	40	200	2.26	-7.3471	1.68	4.09	700.7
	240	60	60	200	2.59	-7.8539	1.9	4.21	841
	240	80	40	250	2.30	-7.6042	2.36	4.47	843
	240	100	50	150	2.65	-7.7478	2.12	4.16	671.1

ratio [24]. The crosssectional macrographs of the bead profile have been seen with the following conditions based on penetration rate, width, aspect ratio, and input heat depicted in Figure 1 by low-frequency pulsing. According to the basis of the macrostructure, it can be assumed that PCGTA welding will produce superior quality welds with no lack of surface or defects on subsurface. It was also observed that using the parameters specified in experiment 8, a 4.4 mm maximum penetration could be reached. The amount of heat necessary to achieve this penetration has been discovered as 843 J/mm [25]. The results showed that in the five experiments, on 4 mm penetration could be obtained by trials 3, 4, 5, 6, 7, 8, and 9. In trial 4, the minimal aspect ratio was 2.25.

4.2. High-Frequency Pulsing. Figure 2 shows the crosssectional macrograph view of the bead profile, as well as their penetration rate, width of weld, aspect ratio, and input heat. On the basis of the macrostructure, it can be assumed that PCGTA welding will produce optimum quality welds with

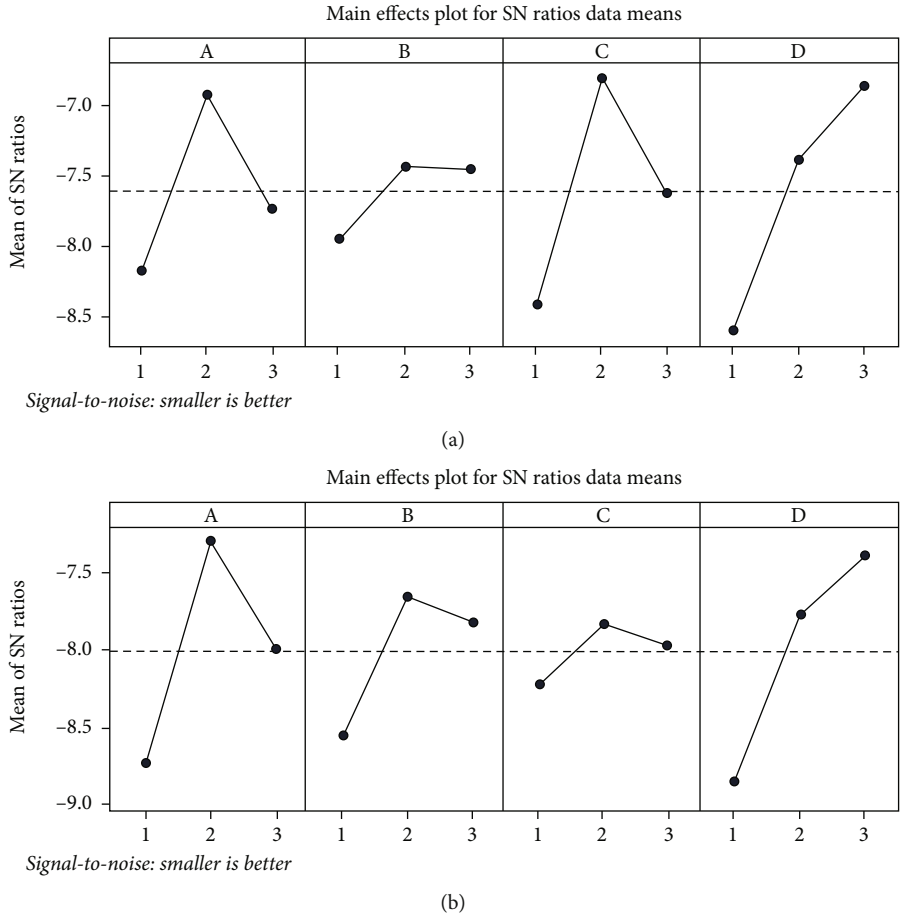

Figure 3: Main effects plot for S/N ratios based on aspect ratios for PC GTAW: (a) high frequency; (b) low frequency.

no surface or subsurface defects [26]. It was also observed that using the parameters specified in experiment 9, the maximum 4.5 mm penetration could be reached. The amount of heat necessary to achieve this penetration was discovered by 838 J/mm. The results showed that in the five experiments, 4 mm penetration rate could be achieved by 2, 3, 4, 6, 7, and 8 trials. In trial 4, there is a minimum aspect ratio of 1.93.

4.3. Taguchi Analysis

4.3.1. S/N Ratio Analysis and Main Effects Plot. In order to obtain the optimal aspect ratio, the results were subjected to a signal to noise ratio study. As previously stated, the superior criterion for aspect ratio was chosen. Tables 3 illustrates the actual S/N ratio values for all the variance with respect to responses [27]. Table 4 shows the Taguchi L9 orthogonal array and experimental results of LF pulsing for bead geometry and their corresponding S/N values and heat inputs. To determine the S/N ratio for each input level, the average of S/N ratios at corresponding levels was determined. Regardless of the criteria, the level-factor with the higher mean S/N ratio was selected as the condition of optimum level input parameter [28].

4.3.2. Low-Frequency Pulsing. Figure 3 represents the main impacts graphs on the S/N ratios. (a) Table 5 shows the response table for the S/N values of aspect ratio. Combination of optimum input level-factors was interpreted by the response table corresponding to main effect plots. The most important parameters that determine the aspect ratio are frequency and peak current [29].

4.3.3. High-Frequency Pulsing. Table 6 depicts the mean S/N values on the aspect ratio (W/P) for each input level parameters, as illustrated in Figure 3. Table 7 shows the optimum parameters for a reduced aspect ratio. When looking at the mean S/N signals in the response table, it is clear that peak percent, frequency, IP, and IB, attained in descending order of significance, had a largest impact on aspect ratio [30]. Table 8 shows the parameter levels that have been optimized.

4.4. Analysis of Variance (ANOVA). ANOVA optimized results for HF pulsing and LF pulsing are shown in Figure 4. The effectiveness and contribution percentage influence of each component on the effect of bead geometry (W/P) - AISI 409L were determined using ANOVA at a 5% level of significance. Frequency had 20.1% influences on aspect ratio, followed by percent peak with a 32.08 percent significance, then peak current percent (20.1 percent), and base current percent (20.1 percent) (7.7 percent). Table 9 shows the ANOVA results for aspect ratio of LF pulsing.

Table 5: Response table: S/N ratios (low-frequency pulse).

Levels	Ip	Ib	%peak	*F*
1	-8.731	-8.551	-8.220	-8.852
2	-7.291	-7.647	-7.822	-7.769
3	-7.988	-7.812	-7.968	-7.389
Delta	1.439	0.904	0.398	1.463
Rank	2	3	4	1

Table 6: Response table: S/N ratios (high-frequency pulse).

Levels	Ip	Ib	%peak	*F*
1	-8.176	-7.952	-8.414	-8.596
2	-6.935	-7.439	-6.808	-7.389
3	-7.735	-7.456	-7.625	-6.863
Delta	1.241	0.513	1.606	1.733
Rank	3	4	2	1

Table 7: Optimized input parameters: lower aspect ratio (AR-HF pulse).

S. no.	Factors	Levels	Values
1	Peak current in amps	2	220
2	Base current in amps	2	80
3	Peak in %	2	50
4	Pulse frequency in HZ	3	250

Table 8: Optimized parameters for lower aspect ratio (AR) in LF pulsing.

S. no.	Factor	Level	Values
1	Peak current in amps	2	220
2	Base current in amps	2	80
3	Peak (%)	2	50
4	Pulse frequency in Hz	3	10

Table 10 shows the ANOVA results for aspect ratio of HF pulsing.

4.5. Analysis of Variance. After the comparison of outcomes related to LF and HF current pulsing approaches, it is clear that in HF-PCGTAW, the arc is better focused when higher welding speeds and frequencies are used. Furthermore, compared to low-frequency pulsed GTA, the HF pulsed GTA technique is better to control over the optimum penetration rate with low input heat. With a heat input of 838 J/mm, they observed a higher depth of 4.5.2 mm [31]. The faster the pulse, the faster the travel speed, and hence, the higher the weld quality. The difference in welding speed between the two procedures is thought to be the reason for this. As a result of the greater frequency, less time is spent welding in a specific spot, lowering the heat input [32]. As a result, HF-PCGTAW saves a significant amount of energy, increasing productivity. The production of undesired phases is limited when the input heat on the fusion zone was reduced, which enhances the weld characteristics. When the comparison on the major effects plots of LF and HF on PCGTAW was discovered by IB plots for both approaches had nearly the same pattern [33]. This is because the effect of base current is limited to maintaining a steady arc. If the peak percent is higher, the present pulse will stay on for a longer time [34]. Because the heat required to melt the parent metal is supplied during the peak pulse, when the peak percent is higher, more heat is delivered. As a result, there is better penetration and a wider bead width. As a result, peak percent is the most influential metric that is also observed [35].

4.5.1. Microstructure of Weld Samples. The plate was sectioned in the transverse direction after welding, and samples were made and polished with different grades of abrasive

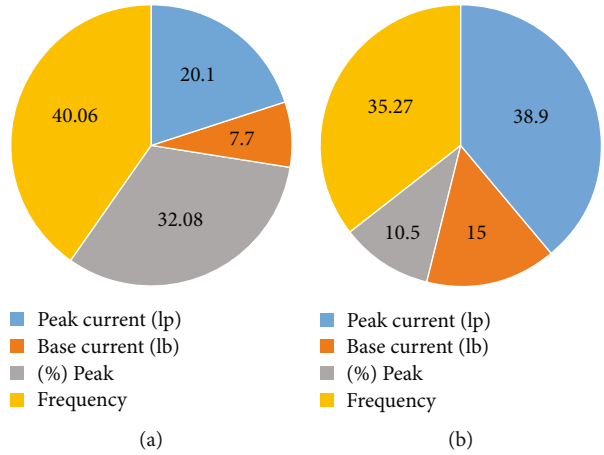

Figure 4: ANOVA optimized results for (a) HF pulsing and (b) LF pulsing.

Table 9: ANOVA results for aspect ratio of LF pulsing.

Sources	DOF	Adj SS	Adj MS	*F* value	*P* value
A	2	0.29416	0.14708	*	*
B	2	0.11402	0.05701	*	*
C	2	0.08069	0.04034	*	*
D	2	0.26642	0.13321	*	*
Error	0	*	*		
Total	8	0.75529			

Table 10: ANOVA results for aspect ratio of HF pulsing.

Sources	DF	Adj SS	Adj MS	*F* value	*P* value
A	2	0.20602	0.10301	*	*
B	2	0.07869	0.03934	*	*
C	2	0.32809	0.16404	*	*
D	2	0.40962	0.20481	*	*
Error	0	*	*		
Total	8	1.02242			

emery sheet; additional polishing was done with diamond polishing using 1 m diamond paste. The samples are polished and etched by Vilella reagent (30%) (3 g picric acid +15 ml hydrochloric acid +200 ml ethanol and dual viewed under a Leica DM750 Microscope.

4.5.2. Microscopic Images for Different Regions. The following are the observations made for a sample for their regions termed parent metal region, heat impacted, and fusion zone. All of the images were taken at a magnification of 50x. As demonstrated in Figure 5, delta-ferrite combined with needle-martensite forms in the pulsed TIG weld fusion zone (d). Because of the autogenous and single-pass heat cycle, a uniform phase distribution throughout the weld of fusion zone has expected in the pulsed TIG weld [36]. The presence of ferrite and martensite in the microstructure is confirmed by the pulsed TIGW fusion zone [37]. The presence of delta-ferrite combined with martensite can be seen in the HA zone of welds.

4.6. Mechanical Properties

4.6.1. Tensile Testing Results. Mico-Vickers hardness and transverse tensile testing has been obtained to compare the characteristics of mechanical parameters of the pulsed TIGW samples. The tensile samples were made as per the standard of ASTM E8 M-04 (gauge length and width of 25 and 6 mm), as illustrated in Figure 6. The tensile test was carried out by a Tinius Olsen universal testing machine with a capacity of 50 KN eletromechanical controlled crosshead speed (strain rate) of 1 mm/min [38]. The tensile strength values of optimized samples, such as ultimate tensile strength and elongation rate, are shown in Table 11.

Pulsed TIG discovered a maximum UTS of 445 MPa and a minimum of 385 MPa. 415 MPa is the average of three

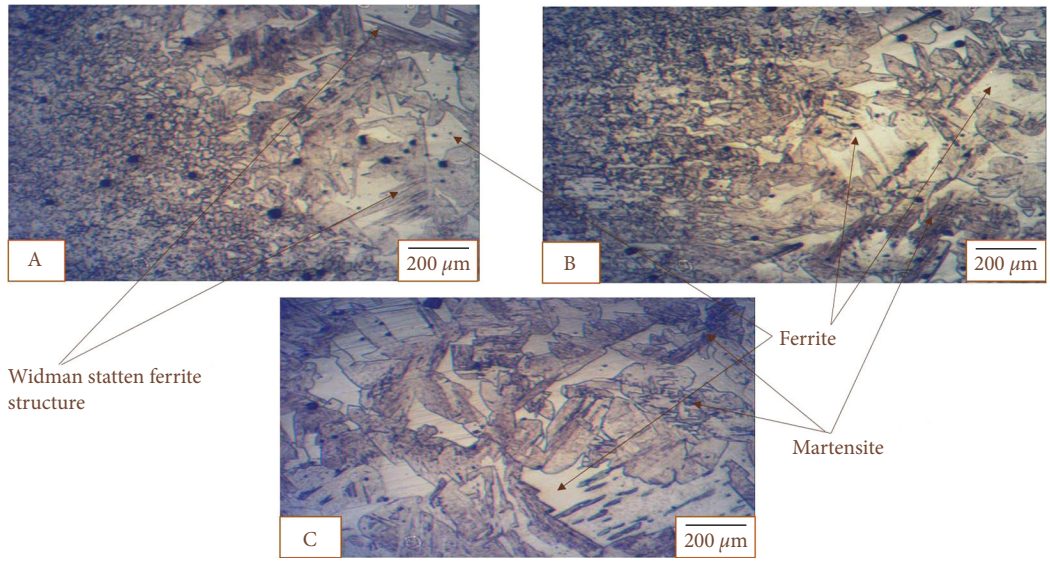

Figure 5: Surface morphology: (a) collective view, (b) HAZ, and (c) pulsed TIG weld.

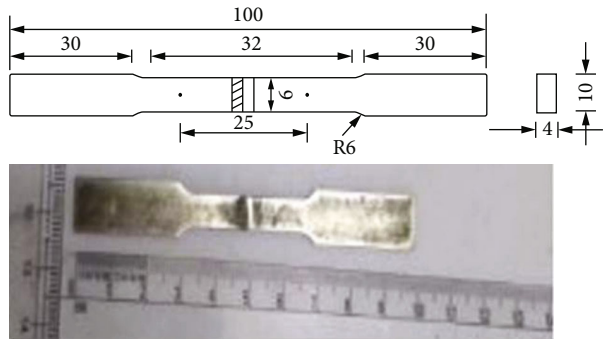

Figure 6: ASTM E8 standard specimen dimensions for tensile testing.

Table 11: Tensile test specimen UTS and % elongation.

Specimen no	Ultimate strength (MPa)	% total elongation
1	445	26.
2	421.4	26.5
3	385	24.2
Average	415	25.56

samples. The welded metal in all joints had a higher UTS compared to parent metal, according to the findings. Despite the fact that all of the samples failed by the parent metal, the samples' strength varies. The percentage strain obtained for both welds, however, was smaller than that of the base metal. The martensitic development was blamed for the higher UTS and decreased ductility of the pulsed TIG welds. Furthermore, the hardness results are consistent with the tensile experiments, as the fusion zone has a higher hardness than the parent metal. AISI 409L by GTAW samples were exhibited more brittle in nature due to the formation of lathe martensite phases which is responsible in increasing material strength [39].

4.6.2. Vickers Microhardness Test. The test conditions are as follows: diamond indenter with a 500-gram load and a 10-second dwell duration. The Vickers microhardness test was conducted in accordance with ASTM E92 standard.

The Vickers hardness of the pulsed TIG weld samples is measured using the Matsuzawa MMTX-7 at KAHE, Tamil Nadu, India, as mentioned in Figure 7. The micro-Vickers hardness number for the welded place ranged from 220 to 270 HV, while the base metal's average hardness was 160 HV. The transformation of microstructure phase from ferritic structure to martensitic structure was attributed to the increased hardness of the pulsed TIG weld zone [40]. The pulsed TIG weld fusion zone had a consistent hardness distribution, with slightly reduced hardness towards the start to the center. In the pulsed TIG weldment, low solidification rate was found on the center of the weld; it results in more grain growth and less martensitic transformation. The transformation to martensitic structure with fine grain refinement was placed via HAZs the weld, which has response for the increased hardness in HA Zone as compared to parent metal. The martensitic transition and grain refinement occurred in the HAZs weld, resulting in improved hardness in HA zone compared to parent metal.

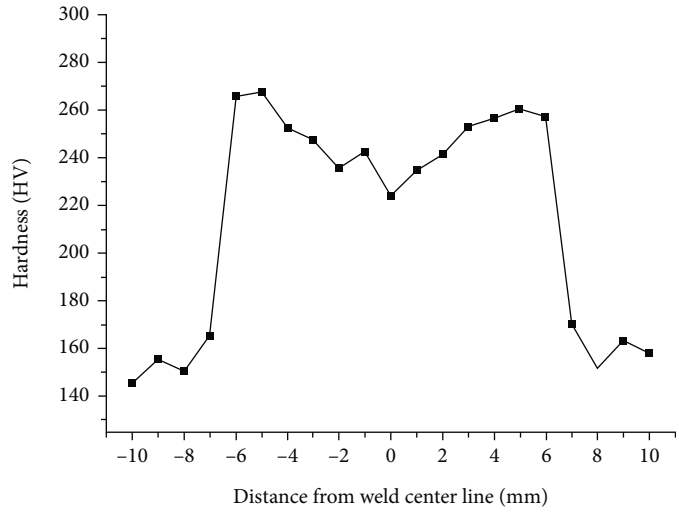

Figure 7: Hardness variation of BM, HAZ, and FZ.

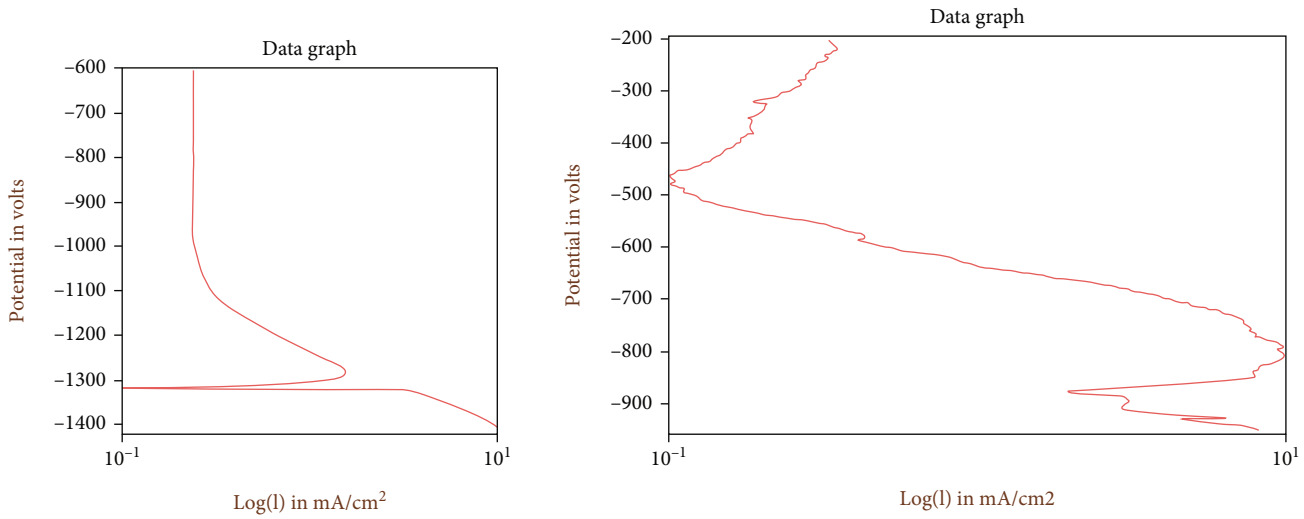

	Corrosion rate (mpy)	Icorr (mA/cm2)
Weld	0.0118299	5.2303
Base metal	0.5170	0.011695

Figure 8: Polarization curve for (a) weld metal and (b) base metal.

4.7. Corrosion Studies

4.7.1. Potentio-dynamic Polarization Test. The corrosion rate is calculated using a potentio-dynamic polarization test for the parent metal and weld region, as seen in Figure 8. The electrochemical corrosion studies were conducted in accordance with ASTM G199–09 standard.

Corrosion tests on the welded samples were carried out using a VersaSTAT 4, (AMETEK, KAHE, Tamil Nadu, India) electrochemical workstation. A three-electrode electrochemical cell system was used in this study. The reference electrode (SSE) was a Ag/AgCl saturated in KCl, and the auxiliary electrode has a platinum electrode. Working electrode was the sample under test. PDP (potentio-dynamic polarization) was used to investigate corrosion and its pace. The 3.5 percent NaCl solution was exposed to a surface area of 0.07065cm^2 of base materials and weld nuggets. The rate of corrosion of the base material is lower than the rate of corrosion of the weld metal. As a result, the corrosion resistance of the base material is larger than the resistance to corrosion of the weld metal. The presence of martensite reduces the resistance to general corrosion, but it also reduces the pitting potential as the martensite content rises. That could be the reason for the decrease in weld metal corrosion resistance.

5. Conclusion

Based on combination of input process parameters IP = 220 amps, Ib = 80 amps, peak percent = 50%, and frequency = 250 Hz, complete penetration of 4.5 mm was accomplished in the pulsed TIG. High-pulsed frequency has a 40.06 percent influence on aspect ratio, followed by percent peak with a relevance of 32.08 percent, peak current percent (20.1 percent), and base current percent (20.1 percent) (7.7 percent). In high-frequency pulsing, frequency has the greatest impact on bead shape, whereas in low-frequency pulsing, peak current (Ip) has the most impact. The pulsed TIG weld fusion zone is where delta ferrite with needle-like martensite forms. It was due to the autogenous with single-pass heat cycle that uniform phase distribution along entire weld fusion zone was imposed in the rate of pulsed TIG weld. The presence of ferrite and martensite in the microstructure is confirmed by the pulsed TIG weld fusion zones. The presence of delta-ferrite combined with martensite structure is seen from the HA zone of welds. Pulsed TIG found a maximum UTS of 440 MPa and a minimum of 392 MPa. 417 MPa is the average of three samples. The weld metal in all of the joints had a greater UTS than the base metal, according to the findings. The basic metal failed all of the samples. The rate of resistance to corrosion of the parent material is lower than the rate of corrosion of the weld metal. As a result, the resistant to corrosion of the parent material is larger than the resistant to corrosion of the welded metal. The presence of martensite reduces the resistance to general corrosion, but it also reduces the pitting potential as the martensite content rises. That could be the reason for the decline in weld metal corrosion resistance.

Data Availability

The data used to support the findings of this study are included in the article. Should further data or information be required, these are available from the corresponding author upon request.

Conflicts of Interest

The authors declare that there are no conflicts of interest regarding the publication of this paper.

Acknowledgments

We thank and acknowledge the management of Saveetha School of Engineering, Chennai, for their support to carry out this research work. The authors appreciate the supports from Ambo University, Ethiopia.

References

[1] M. B. Chennaiah, P. N. Kumar, and K. P. Rao, "Effect of pulsed TIG welding parameters on the microstructure and microhardness of AA6061 joints," *Journal of Materials Science and Engineering*, vol. 4, pp. 4–7, 2015.

[2] M. Shojaati and B. Beidokhti, "Characterization of AISI 304/AISI 409 stainless steel joints using different filler materials," *Construction and Building Materials*, vol. 147, pp. 608–615, 2017.

[3] M. Indira Rani and R. N. Marpu, "Effect of pulsed current TIG welding parameters on mechanical properties of J-joint strength of Aa6351," *The International Journal of Engineering and Science (IJES)*, vol. 1, no. 1, pp. 1–5, 2012.

[4] M. Aghakhani, E. Mehrdad, and E. Hayati, "Parametric optimization of gas metal arc welding process by Taguchi method on weld dilution," *International Journal of Modeling and Optimization*, vol. 1, no. 3, pp. 216–220, 2011.

[5] D. Devakumar and D. B. Jabaraj, "Research on gas tungsten arc welding of stainless steel–an overview," *International Journal of Scientific and Engineering Research*, vol. 5, no. 1, pp. 1612–1618, 2014.

[6] Y. Xie, Y. Cai, X. Zhang, and Z. Luo, "Characterization of keyhole gas tungsten arc welded AISI 430 steel and joint performance optimization," *The International Journal of Advanced Manufacturing Technology*, vol. 99, no. 1-4, pp. 347–361, 2018.

[7] B. Kumar, C. P. Swarup Bag, C. R. Paul, R. R. Das, and K. S. Bindra, "Influence of the mode of laser welding parameters on microstructural morphology in thin sheet Ti6Al4V alloy," *Optics & Laser Technology*, vol. 131, p. 106456, 2020.

[8] P. Shah and C. Agrawal, "A review on twin tungsten inert gas welding process accompanied by hot wire pulsed power source," *Journal of Welding and Joining*, vol. 37, no. 2, pp. 41–51, 2019.

[9] W. Wu, H. Shengsun, J. Shen, L. Ma, and J. Han, "Sensitization of 21% Cr ferritic stainless steel weld joints fabricated with/without austenitic steel foil as interlayer," *Journal of Materials Engineering and Performance*, vol. 24, no. 4, pp. 1505–1515, 2015.

[10] D. Patel and S. Jani, "Techniques to weld similar and dissimilar materials by ATIG welding-an overview," *Materials and Manufacturing Processes*, vol. 36, no. 1, pp. 1–16, 2021.

[11] S. Yogeshwaran, L. Natrayan, S. Rajaraman, S. Parthasarathi, and S. Nestro, "Experimental investigation on mechanical properties of epoxy/graphene/fish scale and fermented spinach hybrid bio composite by hand lay-up technique," *Materials Today: Proceedings*, vol. 37, pp. 1578–1583, 2021.

[12] K. Seeniappan, B. Venkatesan, N. N. Krishnan et al., "A comparative assessment of performance and emission characteristics of a DI diesel engine fuelled with ternary blends of two higher alcohols with lemongrass oil biodiesel and diesel fuel," *Energy & Environment*, vol. 13, p. 0958305X2110513, 2021.

[13] D. Zhao, Y. Bezgans, N. Vdonin, and D. Wenhao, "The use of TOPSIS-based-desirability function approach to optimize the balances among mechanical performances, energy consumption, and production efficiency of the arc welding process," *The International Journal of Advanced Manufacturing Technology*, vol. 112, no. 11-12, pp. 3545–3559, 2021.

[14] S. C. Moi, P. K. Pal, A. Bandyopadhyay, and R. Rudrapati, "Determination of tungsten inert gas welding input parameters to attain maximum tensile strength of 316L austenitic stainless steel," *Mechanical Engineering*, vol. 68, no. 3, pp. 231–248, 2018.

[15] P. Babu Aurtherson, J. Hemanandh, Y. Devarajan, R. Mishra, and B. C. Abraham, "Experimental testing and evaluation of coating on cables in container fire test facility," *Nuclear Engineering and Technology*, vol. 54, no. 5, 2022.

[16] Y. Devarajan, B. Nagappan, G. Choubey, S. Vellaiyan, and K. Mehar, "Renewable pathway and twin fueling approach

on ignition analysis of a dual-fuelled compression ignition engine," *Energy & Fuels*, vol. 35, no. 12, pp. 9930–9936, 2021.

[17] A. K. Lakshminarayanan, K. Shanmugam, and V. Balasubramanian, "Effect of autogenous arc welding processes on tensile and impact properties of ferritic stainless steel joints," *International*, vol. 16, no. 1, pp. 62–68, 2009.

[18] W. Wu, H. Shengsun, and J. Shen, "Microstructure, mechanical properties and corrosion behavior of laser welded dissimilar joints between ferritic stainless steel and carbon steel," *Materials & Design*, vol. 65, pp. 855–861, 2015.

[19] P. Asha, L. Natrayan, B. T. Geetha et al., "IoT enabled environmental toxicology for air pollution monitoring using AI techniques," *Environmental Research*, vol. 205, p. 112574, 2022.

[20] J. Verma and R. V. Taiwade, "Effect of welding processes and conditions on the microstructure, mechanical properties and corrosion resistance of duplex stainless steel weldments–a review," *Journal of Manufacturing Processes*, vol. 25, pp. 134–152, 2017.

[21] Y. Devarajan, G. Choubey, and K. Mehar, "Ignition analysis on neat alcohols and biodiesel blends propelled research compression ignition engine," *Energy Sources, Part A: Recovery, Utilization, and Environmental Effects*, vol. 42, no. 23, pp. 2911–2922, 2020.

[22] R. Shanmugam, D. Dillikannan, G. Kaliyaperumal, M. V. De Poures, and R. K. Babu, "A comprehensive study on the effects of 1-decanol, compression ratio and exhaust gas recirculation on diesel engine characteristics powered with low density polyethylene oil," *Energy Sources, Part A: Recovery, Utilization, and Environmental Effects*, vol. 43, no. 23, pp. 3064–3081, 2021.

[23] W. Chuaiphan and L. Srijaroenpramong, "Effect of welding speed on microstructures, mechanical properties and corrosion behavior of GTA-welded AISI 201 stainless steel sheets," *Journal of Materials Processing Technology*, vol. 214, no. 2, pp. 402–408, 2014.

[24] L. Natrayan, V. Sivaprakash, and M. S. Santhosh, "Mechanical, microstructure and wear behavior of the material AA6061 reinforced SiC with different leaf ashes using advanced stir casting method," *International Journal of Engineering and Advanced Technology*, vol. 8, pp. 366–371, 2018.

[25] R. Adhinarayanan, A. Ramakrishnan, G. Kaliyaperumal, M. V. De Poures, R. K. Babu, and D. Dillikannan, "Comparative analysis on the effect of 1-decanol and di-n-butyl ether as additive with diesel/LDPE blends in compression ignition engine," in *Energy Sources, Part A: Recovery, Utilization, and Environmental Effects*, pp. 1–18, Taylor and Francis Ltd., United Kingdom, 2020.

[26] T. R. Dandekar, A. Gupta, A. Kumar, R. K. Khatirkar, and B. Vadavadagi, "Shielded metal arc welding of UNS S32750 steel: microstructure, mechanical properties and corrosion behaviour," *Materials Research Express*, vol. 5, no. 10, p. 106506, 2018.

[27] C. B. Durtewitz and F. Almeraya Calderón, "Electrochemical corrosion of ferritic 409 and 439 stainless steels 409 and 439 in NaCl and H2SO4 solutions," *International Journal of Electrochemical Science*, vol. 11, pp. 1080–1091, 2016.

[28] H. He, W. Chuansong, S. Lin, and C. Yang, "Pulsed TIG welding–brazing of aluminum–stainless steel with an Al-Cu twin hot wire," *Journal of Materials Engineering and Performance*, vol. 28, no. 2, pp. 1180–1189, 2019.

[29] G. Lothongkum, P. Chaumbai, and P. Bhandhubanyong, "TIG pulse welding of 304L austenitic stainless steel in flat, vertical and overhead positions," *Journal of Materials Processing Technology*, vol. 89-90, pp. 410–414, 1999.

[30] P. K. Ghosh and R. Kumar, "Surface modification of microalloyed high-strength low-alloy steel by controlled TIG arcing process," *Metallurgical and Materials Transactions A*, vol. 46, no. 2, pp. 831–842, 2015.

[31] N. Karunakaran, "Effect of pulsed current on temperature distribution, weld bead profiles and characteristics of GTA welded stainless steel joints," *International Journal of Engineering and Technology*, vol. 2, no. 12, 2011.

[32] N. Chandrasekhar, M. Ragavendran, R. Ravikumar, M. Vasudevan, and S. Murugan, "Optimization of hybrid laser–TIG welding of 316LN stainless steel using genetic algorithm," *Materials and Manufacturing Processes*, vol. 32, no. 10, pp. 1094–1100, 2017.

[33] D. Yuvarajan, M. Venkata Ramanan, and D. Christopher Selvam, "Performance analysis on mustard oil methyl ester as a potential alternative fuel," *Journal of Science and Technology*, vol. 9, no. 37, 2016.

[34] B. J. Qi, M. X. Yang, B. Q. Cong, and F. J. Liu, "The effect of arc behavior on weld geometry by high-frequency pulse GTAW process with 0Cr18Ni9Ti stainless steel," *The International Journal of Advanced Manufacturing Technology*, vol. 66, no. 9-12, pp. 1545–1553, 2013.

[35] K. Hemalatha, C. James, L. Natrayan, and V. Swamynadh, "Analysis of RCC T-beam and prestressed concrete box girder bridges super structure under different span conditions," *Materials Today: Proceedings*, vol. 37, pp. 1507–1516, 2021.

[36] P. R. Vishnu and K. E. Easterling, *Phenomenological modelling of heat flow and microstructural changes in pulsed GTA [TIG] welds in a quenched and tempered steel*, pp. 241–300, Institute of Materials, London, 1993.

[37] M. Moradi, M. Ghoreishi, and A. Rahmani, "Numerical and experimental study of geometrical dimensions on laser-TIG hybrid welding of stainless steel 1.4418," *Journal of Modern Processes in Manufacturing and Production*, vol. 5, no. 2, pp. 21–31, 2016.

[38] V. Balaji S. Kaliappan et al., "Combustion analysis of biodiesel-powered propeller engine for least environmental concerns in aviation industry," *Aircraft Engineering and Aerospace Technology*, vol. 94, no. 5, pp. 760–769.

[39] A. K. Singh, V. Dey, and R. N. Rai, "Techniques to improve weld penetration in TIG welding (a review)," *Materials Today: Proceedings*, vol. 4, no. 2, pp. 1252–1259, 2017.

[40] S. Rathinam, K. Balan, G. Subbiah, J. Sajin, and Y. Devarajan, "Emission study of a diesel engine fueled with higher alcohol-biodiesel blended fuels," *International Journal of Green Energy*, vol. 16, no. 9, pp. 667–673, 2019.